Acta Astronautica 178 (2021) 908–919

Contents lists available at ScienceDirect

Acta Astronautica

journal homepage: www.elsevier.com/locate/actaastro

Epoxy-based shape memory composite for space applications

Debby Margoy [a,b], Irina Gouzman [a], Eitan Grossman [a], Asaf Bolker [a], Noam Eliaz [b], Ronen Verker [a,*]

[a] Space Environment Department, Soreq NRC, Yavne, 81800, Israel
[b] Department of Materials Science and Engineering, Tel-Aviv University, Tel Aviv, 6997801, Israel

ARTICLE INFO

Keywords:
Shape memory polymer
Space environment
Actuator

ABSTRACT

Shape memory polymers are smart materials with an ability to recover their permanent shape from a temporary shape upon exposure to various external stimuli. In space applications, shape memory polymers can find their use as deployable devices due to their high strength-to-weight ratio and large deformability. The effect of vacuum environment in space on the deployment of shape memory polymers is an extremely important issue which is yet to be studied. As the energy budget in spacecraft is limited, means to increase the energetic efficiency of deployable devices need to be developed.

In this work, shape memory polymer actuators based on carbon resistive heating fibers and epoxy matrix were developed for space applications. Their mechanical, thermal, and electrical properties, as well as their deployment kinetics at both ambient and vacuum conditions, were studied. A method for improvement of the deployment energetic efficiency of shape memory polymer actuators, based on aluminum coating for internal radiative heating, was introduced. An innovative technique, which provides motion sensing at the first stage of the shape memory polymer actuators deployment, was demonstrated. This technique uses the resistive heating characteristics of carbon fibers and *in situ* electrical resistance drop during deployment. Finally, the durability of the shape memory polymers actuators in the space environment was discussed.

1. Introduction

Under the severe space conditions, the use of advanced, durable, and lightweight materials is highly desirable [1–7]. Spacecraft orbiting the Earth are exposed to severe environmental conditions, which combine ultrahigh vacuum (UHV), hypervelocity impacts by micrometeoroids and debris, extreme temperature cycles of the order of −100 °C to +100 °C, and ultraviolet (UV) and ionizing radiation. Some environmental conditions vary according to the spacecraft's orbit, i.e. altitude and inclination. In geosynchronous Earth orbit (GEO), at an altitude of 36,000 km, spacecraft are exposed to high fluxes of charged particles and ionizing radiation. In low Earth orbit (LEO) altitudes of 200–700 km, spacecraft are also exposed to hazards such as atomic oxygen (AO) [8–11]. Shape memory polymers (SMPs) are good candidates for specific applications in spacecraft, mainly due to their low density, large recoverable strain, and long recovery time, which results in small impact in spacecraft release mechanisms. As such, SMPs can replace heavy metal-based mechanisms in spacecraft [12–14]. Recently, SMPs have shown energy output values of the order of few MJ/m^3, comparable to shape memory alloys (SMAs) [15]. In terms of the actuation force-to-weight ratio, SMPs show at least one order of magnitude lower ratio than SMAs [16]. SMPs are stimuli-responsive materials that after being deformed can return to their pre-deformed shape by application of external stimuli, such as light, heat, electric or magnetic fields, pH level, or ionic strength. The shape memory material "remembers" its previous shape [17,18]. The shape memory effect (SME) in SMPs results from a combination of the polymer structure and morphology together with the applied processing and programming technology. SMP is an elastic polymer network that underlies active movement. The polymer network consists of the molecular switching segment and net-point hard segments. The net-points determine the permanent shape of the polymer network, and can be of either chemical (covalent bonds) or physical (intermolecular interactions) in nature. The molecular switches can reduce their stiffness with a particular stimulus, allowing the polymer to be programmed into its temporary shape. Upon exposure to a specific stimulus, the molecular switches are triggered, and strain energy stored in the temporary shape is released, resulting in shape recovery [19,20]. In the past, research mainly focused on thermoplastic SMPs. Unfortunately, the structures made of thermoplastic SMPs lose their SME after

* Corresponding author.
E-mail address: rverker@soreq.gov.il (R. Verker).

https://doi.org/10.1016/j.actaastro.2020.08.026
Received 6 June 2020; Received in revised form 16 July 2020; Accepted 20 August 2020
Available online 27 August 2020

Abbreviations list

AO	- atomic oxygen
CFs	- carbon fibers
CTE	- coefficient of thermal expansion
DIC	- digital image correlation
DMA	- dynamic mechanical analysis
EBPVD	- electron beam physical vapor deposition
GEO	- geosynchronous Earth orbit
HRSEM	- high-resolution scanning electron microscope
LEO	- low Earth orbit
MFP	- mean free path
PAN	- polyacrylonitrile
PTC	- positive temperature coefficient
RT	- room temperature
SMAs	- shape memory alloys
SME	- shape memory effect
$SMPA_{Al}$	- aluminum-coated shape memory polymer actuator
SMPAs	- shape memory polymer actuators
$SMPA_{U}$	- epoxy-carbon fiber uncoated shape memory polymer actuator
SMP_{R}	- epoxy SMP
SMPs	- shape memory polymers
UHV	- ultrahigh vacuum
UV	- ultraviolet

several cycles. Therefore, thermoset SMPs with high material stiffness, high glass transition temperature ($T_g > \sim 100$ °C), and excellent environmental durability are becoming an attractive alternative for the manufacturing of space structures [21–23]. Thermoelectric-triggered SMPs, i.e. SMPs triggered by resistive heating, are promising candidates for space applications because other triggering mechanisms, e.g. pH or humidity, are not relevant in the space environment [24].

Space applications require motion indication of SMP-based elements beyond visual line-of-sight. Motion and strain measurements of SMPs can be performed nowadays directly through contact methods such as extensometers and strain gauges, or indirectly through non-contact methods such as laser extensometer, videometry, and digital image correlation (DIC). The use of these non-contact methods is not relevant for space applications mainly due to weight issues and technological complications. The use of the aforementioned contact methods is limited by the low strain (~20%) these methods can measure compared to the extremely high strain (~100%) that SMPs can endure [25,26]. Another important direct contact method for strain measurement is based on optical fiber sensors, e.g. fiber Bragg grating. These sensors are immune to electromagnetic disturbance and resist harsh environmental conditions [27,28].

One of the most attractive thermoelectric-triggered SMPs is epoxy adhesive [21]. Epoxy-based SMPs are highly attractive for space applications due to their low outgassing properties, high triggering temperature, and high strength-to-weight ratio [22]. Epoxy SMPs exhibit a shape recovery ratio of 98–100% and an elastic modulus of 1.5–3.5 GPa. In addition, they perform well when exposed to space radiation. Epoxy can be used as a matrix reinforced by carbon fibers (CFs) for composite applications, such as hinges, solar arrays, deployable panels, booms, and reflector-antennas [19]. Epoxy also has high resistance to wear, and its surface is relatively hard due to its aromatic segments. It also has high adhesion to metals due to its polarity. Reinforcement with graphite, carbon particles, or fibers can largely improve its strength and stiffness [17,18].

Nevertheless, the effect of the space environment, especially UHV, on the deployment kinetics and energy consumption of epoxy-based SMPs, reinforced with carbon, is not fully understood. The space industry, universities, and research institutes have expanded their research and development activities nowadays toward the so-called New Space projects that are based mostly on nanosatellites [29,30]. However, the low mass and restricted solar panels area of nanosatellites limit their power budget [31,32]. It is therefore of high importance to find means to produce SMP actuators (SMPAs) with extremely low power for their deployment. This will enable their extensive integration into satellites in general, and into nanosatellites in particular [24].

In this study, SMPAs that are based on an epoxy matrix and a single imbedded CF yarn used for resistive heating, mechanical reinforcement, and motion sensing, were developed. The CF yarn was embedded in the matrix in a w-like architecture, i.e. both ends of the yarn were on the same side of the SMPA. This architecture can promote the usage of these SMPAs in future mechanical designs. CFs are widely used for reinforcement of epoxy-based composites in automotive, aviation, and space applications [33,34] mainly due to their excellent fiber-matrix interface strength [35] and superior mechanical properties, as well as their thermal stability. An important advantage of CF yarns is their ability to be shaped into complex contours, such as u-shapes with a bending radius in the millimeters range [36]. CF yarns were chosen due to a combination of their unique mechanical properties on one hand, and their thermal and electrical properties that enable them to be used as an effective heating element, on the other hand [37–39]. Though compared to conventional composites, the SMPAs used in this work had low CF volume fraction, their ability to reinforce the matrix was substantial. The deployment kinetics of SMPAs was investigated under various environmental conditions. A novel method for the improvement of their power efficiency during deployment using an aluminum thermal coating was demonstrated. Finally, means for sensing the SMPAs' motion through measurement of the electrical resistance of the CF was demonstrated, and a phenomenological model, which explains our findings, was proposed.

2. Experimental

2.1. Materials

The adhesive for the SMPA was prepared from Epon™ 826 DGEBA resin (Momentive, Inc.) and Jeffamine® D230 poly(propylene glycol)bis (2-aminopropyl) ether crosslinker agent (Huntsman Chemicals, Inc.). The chemical structures of these materials are shown in Fig. 1. In

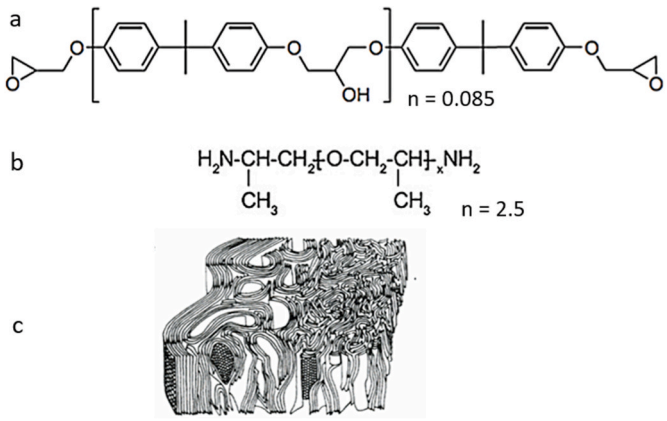

Fig. 1. Molecular structure of (a) Epon 826 resin, (b) Jeffamine D230 polyetheramine crosslinker. (c) Schematics of a PAN-based carbon fiber structure (Wiley©) [40].

addition, 3k-70-p (type 2, grade 3, class 1) polyacrylonitrile (PAN)-based T300 CF yarn (Hexcel Inc.) was used. Each yarn is composed of 3000 CF filaments having an average diameter of 7.6 ± 0.4 μm.

2.2. Sample preparation

Three types of epoxy-based SMPs and SMPAs were prepared using an aluminum mold. When CFs were immersed into the cavity and adhesive was poured above, the samples are denoted as SMPAs. Without CFs, the samples are denoted as SMPs. The materials used to prepare the various SMPs and SMPAs in this work are summarized in Table 1. The three types of samples are denoted as SMP_R for pure epoxy SMP (used as a reference), $SMPA_U$ for epoxy-CF uncoated SMPA, and $SMPA_{Al}$ for aluminum-coated SMPA.

Epoxy resin was mixed with the crosslinker agent in a volume ratio of 2.52:1, respectively [41]. Both materials were preheated before mixing to 50 °C and were added to a vial. The vial was first shaken vigorously by hand, and then by Vortex shaker for 1 min at 30 rpm. Next, the vial was placed in a vacuum oven, which was preheated to 50 °C, for degassing at a pressure of less than 10 mmHg. After 13 min, the vial was taken out, and the adhesive was poured into the mold.

Before pouring the adhesive, the molds with inner dimensions of 70 mm length, 10 mm width and 1–1.2 mm thickness, were coated with a Watershield™ release agent (Zyvax, Inc.). In the next stage, when SMPAs were prepared, each of the two ends of a single 260 mm long CF yarn was connected to an electrical wire through compression of a heat-shrink tube, and the wires were loaded by a 50 g weight. The CF yarn was then formed in a w-like architecture using a jig with three winding pins. The position of the winding pins was designed to make the CF yarn path four times along the sample at equal spacing across it, and to be covered by the epoxy adhesive from all directions. Next, while the CF yarn was kept in place by the jig, and the fibers were under tension by the weights, 0.8–0.9 mL of the adhesive was poured into each mold. The epoxy adhesive was thermally cured at 100 °C for 1.5 h and post-cured at 130 °C for another 1 h [41]. Upon completion of curing, the mold was cooled to room temperature (RT), and the SMPs and SMPAs were removed from the mold. Using this process, the volume fraction of the CFs was 0.06 per SMPA. Fig. 2a depicts the $SMPA_U$ scheme, including the CF resistive heaters' w-like architecture. Resistive heating of the SMPAs was performed by attaching the SMPA's electrical wires to a current source. Some of the samples ($SMPA_{Al}$) were coated with 100 ± 5 nm thick aluminum coating, as schematically illustrated in Fig. 2b. The coating was performed using electron beam physical vapor deposition (EBPVD) at 1 Å/s deposition rate, pressure of 2×10^{-6} Torr, and RT. The thickness of the coating was measured using a profilometer (model XP200 from Ambios). Fig. 2c depicts the SMP_R scheme.

2.3. Characterization techniques

In order to assess the SME of the SMPAs, they were subjected to the following: 1) Heating to a temperature above T_g, 2) bending the SMPAs from their planar permanent shape to a bended temporary shape, 3) cooling to RT while keeping the SMPAs in their temporary bended shape, 4) reheating and recovering back to the original planar shape. The initial heating of the SMPAs, bending to the temporary shape, and cooling afterwards were performed using a universal testing system (model 3365 from Instron®), equipped with an environmental chamber and a 100 N load cell. The reheating of the SMPAs was performed through resistive heating after mounting the samples on a sample holder outside the universal testing system. The resistive heating current was increased gradually at a rate of 30 mA/min to avoid uneven heat distribution and, as a result, uneven strains that can lead to local failures. The temporary shape is considered as the shape of the deflected samples after the cooling stage. Any shape after reheating and during the transition from the temporary bended shape to the planar permanent shape is considered here as an intermediate shape. The SMPA samples were deformed to a u-like temporary shape using three-point bending grips. The bending was performed by using a 22.8 mm radius loading nose, see Fig. 3a. The samples were bended to a maximum strain of 3.2% at 0.4 mm/min crosshead speed and 42 mm support span. 3.2% strain is equivalent to 9.5 mm deflection, according to Equation (1) [42]:

$$\varepsilon = \frac{6Dd}{L^2} \times 100 \tag{1}$$

where ε (%) is the strain, D (mm) is the deflection, d (mm) is the thickness of the sample, and L (mm) is the support span.

The SME of the SMPAs was measured during the recovery stage, either at ambient pressure or in a vacuum environment (5.5×10^{-4} Torr) using resistive heating by gradually increasing the current at a rate of 30 mA/min, until SME was obtained. The recovery effect was recorded by a video camera, and the images were quantified according to the change in the recovery angle ($\Delta\theta$) and deflection (D), see Fig. 3b. As the current was manually increased, the error in t, resistance, and power measurements derived mainly from the electrical current stabilizing time. The error bars of $\Delta\theta$ and $d\theta/dt$ were obtained from the standard deviation of three measurements. $\Delta\theta$ is calculated according to:

$$\Delta\theta = \theta_t - \theta_i \tag{2}$$

where θ_t and θ_i are the deployment angle at the temporary and intermediate shapes, respectively. At $t = 0$, $\Delta\theta = 0°$ and $D = D_{max}$.

Based on the deflection data that was acquired from the universal testing system during bending and video recording during the recovery stage, the fixity (R_f) and recovery (R_r) ratios were calculated. These values reflect the shape-memory capability. R_f describes the ability of an SMP sample to be fixed in its temporary shape, while R_r reflects the ability of the sample to return to its original permanent shape. R_f and R_r were calculated according to Ref. [43–45], see equation (3) and (4):

$$R_f(N) = \frac{\varepsilon_u(N)}{\varepsilon_m} \tag{3}$$

$$R_r(N) = \frac{\varepsilon_m - \varepsilon_p(N)}{\varepsilon_m - \varepsilon_p(N-1)} \tag{4}$$

where ε_u is the strain upon load removal, ε_m is the SMP strain in its temporary shape while under load, ε_p is the residual strain upon full recovery to the permanent shape, and N is the cycle number.

The Young's moduli of the $SMPA_U$ and SMP_R samples were obtained using the same three-point bending setup that was used during the initial heating and bending stages. Five repetitions were performed for each measurement for determination of the standard deviation. Bending tests were performed either at RT or at 130 °C. The samples were bended at 0.4 mm/min crosshead speed and 42 mm support span. After bending, the environmental chamber was cooled to RT.

The force generated by the $SMPA_U$ during its recovery under resistive heating conditions was measured using the universal testing system. The loading nose remained in a static position while the sample was gradually heated by increasing the current at a rate of 30 mA/min. The force exerted by the $SMPA_U$ on the loading nose was recorded in respect to the current and temperature.

T_g and the glassy-to-rubbery transition region of the epoxy were

Table 1
Composition of the epoxy-based shape memory polymers and shape memory polymers actuators.

Sample denotation	Epon™ 826 (wt.%)	Jeffamine® D230 (wt.%)	CFs	Aluminum coating
Epoxy–reference (SMP_R)	75.5	24.5	–	–
Epoxy–CF ($SMPA_U$)	75.5	24.5	✓	–
Aluminum–coated Epoxy–CF ($SMPA_{Al}$)	75.5	24.5	✓	✓

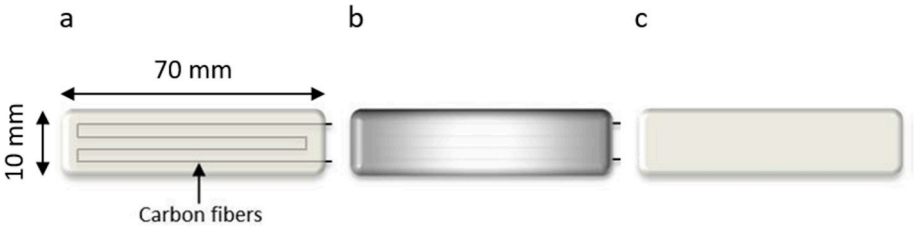

Fig. 2. Schematics of (a) $SMPA_U$ (including carbon fiber yarn resistive heater with a w-like architecture), (b) $SMPA_{Al}$, and (c) SMP_R.

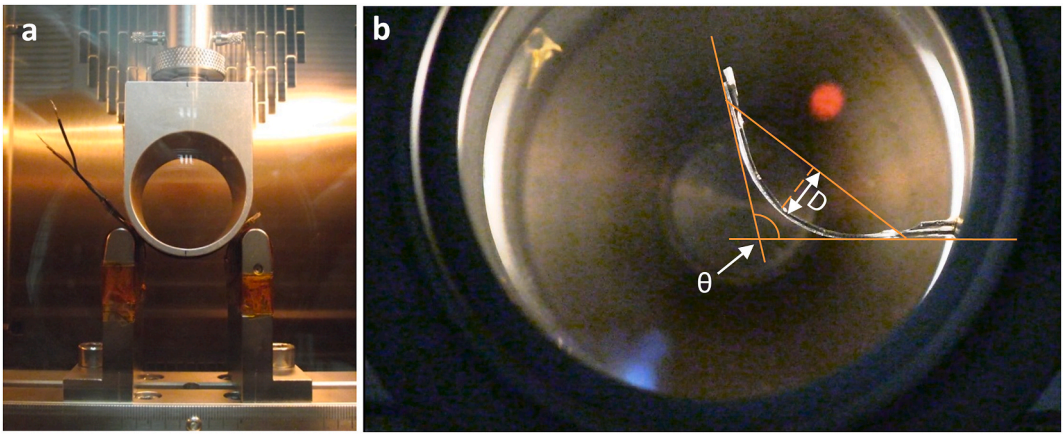

Fig. 3. (a) Bending of a shape memory polymer actuator by Instron® machine at 130 °C. (b) Recovery parameters superimposed on a shape memory polymer actuator installed in a vacuum chamber.

obtained from *tan δ* and storage modulus (*E'*) measurements, using dynamic mechanical analysis (DMA) (model Q800 from TA). The experiments were carried out under multi-frequency mode at a constant amplitude of 0.1% strain using a single frequency of 1 Hz. Temperature scans were performed at 3 °C/min, from 30 to 150 °C, under a nitrogen environment. The T_g was obtained from the *tan δ* peak vs. temperature curve. The glassy-to-rubbery transition region was determined from the onset and offset of E' vs. temperature.

The SMP samples were characterized by a high-resolution scanning electron microscope (HRSEM), model Sigma 300 VP from Zeiss. Images were collected in a variable pressure mode, which enabled measurements of the insulating samples without the application of a conductive coating.

3. Results and discussion

3.1. $SMPA_U$ and SMP_R - shape memory effect and mechanical properties

Table 2 presents Young's modulus data of $SMPA_U$ and SMP_R measured at RT and at 130 °C. At RT, the Young's modulus of the $SMPA_U$ is 2.7 times higher compared to the Young's modulus of the SMP_R, 6.0 GPa vs. 2.2 GPa, respectively. At 130 °C, i.e. above T_g, the values decrease. However, at this elevated temperature, the Young's modulus of the $SMPA_U$ is 104 times higher compared to the Young's modulus of the SMP_R, 1.4 GPa vs. 0.013 GPa, respectively. These results demonstrate the ability of the CF to substantially reinforce the epoxy matrix in spite of its small volume fraction (0.06). Fig. 4 depicts the thermo-mechanical properties (E' and *tan δ*) of an SMP_R sample measured using DMA (Fig. 4a), force generated by the $SMPA_U$ during resistive heating (Fig. 4b), a visual description of the shape recovery of an $SMPA_U$ (Fig. 4c–f), and R_f and R_r during 10 sequential bending and recovery cycles of the $SMPA_U$ (Fig. 4g).

Table 2
Young's modulus of $SMPA_U$ and SMP_R at room temperature and at 130 °C.

Sample	SMP_R	$SMPA_U$	SMP_R	$SMPA_U$
Temperature [°C]	RT	RT	130	130
Young's modulus [GPa]	2.2 ± 0.1	6.0 ± 0.6	0.013 ± 0.001	1.4 ± 0.4

The T_g value of the SMP_R, obtained from the DMA's *tan δ* peak is 102 °C. However, the minimum E' value is received within the rubbery region at a temperature of 130 °C, where bending of the $SMPA_U$ is expected to be flawless, i.e., no fracture or deboning between the matrix and the CF is expected.

Fig. 4b presents the force generated by an $SMPA_U$ sample that was bended to a temporary shape, cooled down to RT, and reheated using resistive heating while the loading nose remained static. The force is presented as a function of the applied current and the temperature developed. The force applied by $SMPA_U$ on the loading nose increased gradually from 0 to 0.12 N, until a temperature of 87 °C was reached. As the temperature increased and T_g was reached, an abrupt increase in the force was observed, reaching 0.85 N. The average weight of an $SMPA_U$ sample was 1.05 g. Therefore, the maximum force-to-weight ratio attained for the $SMPA_U$ sample was 0.77 N/g.

In the first stage of the shape recovery test, as mentioned at the beginning of Section 2.3, the $SMPA_U$ was heated to 130 °C, i.e. above T_g. In the second stage, the $SMPA_U$ was bent to $\theta_t = 53°$. In the third stage, the $SMPA_U$ was cooled to RT, released from the universal testing system, and was attached to a sample holder, see Fig. 4c. During the shape recovery stage (fourth stage), the SME was obtained by resistive heating under ambient pressure conditions. 3 min from the beginning of heating, θ_i equaled θ_t, as the $SMPA_U$ temperature was still below its T_g, see Fig. 4d. 6 min from the beginning of heating, the temperature was above T_g, SME started, and θ_i was recorded as 31°, see Fig. 4e. Almost full recovery was accomplished after 7 min, using a resistive heating current of 210 mA, see Fig. 4f. After the permanent planar shape was reached, the $SMPA_U$ was cooled to RT. A video recording of the $SMPA_U$ deployment process can be found in Video 1 in the supporting information. During 10 bending-recovery cycles (Fig. 4g), the $SMPA_U$ returned almost entirely to its permanent straight shape. The R_r during these cycles was

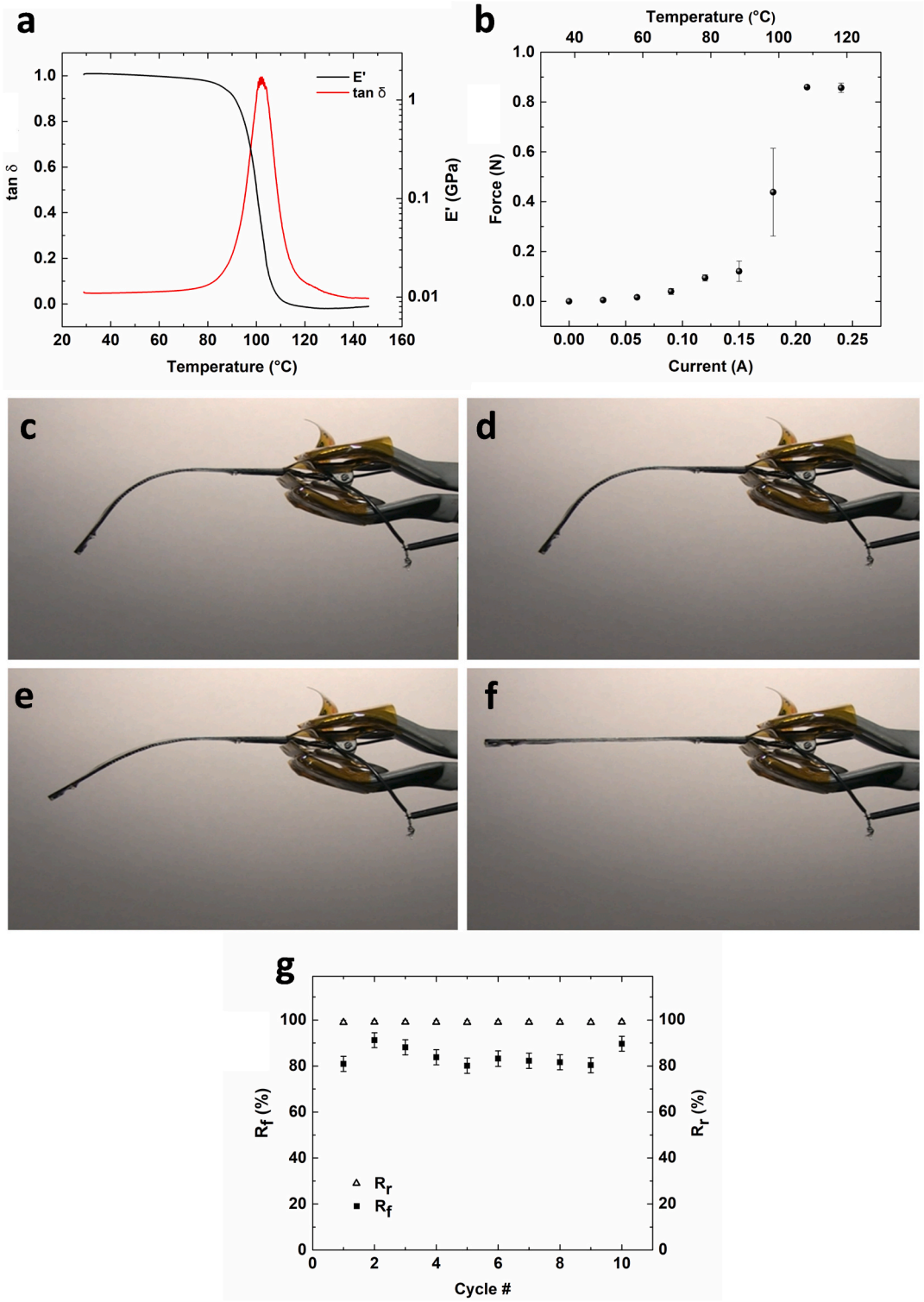

Fig. 4. (a) E' and *tan* δ dynamic mechanical analyzer curves for the SMP_R sample. (b) Force generated by the $SMPA_U$ during the recovery stage. Macroscopic shape memory effect by resistive heating at ambient pressure conditions of $SMPA_U$ sample. (c) Beginning of test, $SMPA_U$ in its temporary shape ($\theta_t = 53°$). (d,e) 3 min ($\theta_t = \theta_i = 53°$) and 6 min ($\theta_i = 31°$), respectively, from the beginning of the resistive heating. (f) Full deployment to the permanent shape. (g) R_f and R_r values during 10 sequential bending and recovery cycles of the $SMPA_U$.

practically constant (98.9–99.1%), and the average R_r value was 99 ± 0.1%. The R_f values during the cycles were between 80% and 91%, with an average of 84 ± 3.6%. These values are somewhat smaller compared to previous work that used the same epoxy, but with no additives [41]. However, as the $SMPA_U$ is made with built-in CFs, which are stiffer than the epoxy matrix, this R_f value may be expected.

Supplementary video related to this article can be found at

3.2. SMPA motion sensing through electrical resistance measurements

During bending and shape memory recovery of the SMPA, changes of the electrical resistance in the permanent and the temporary shapes, as

well as at various temperatures, were observed. Hence, it was decided to study the correlation between bending and temperature, as well as the electrical resistance of the actuators. Such a correlation may be used in future space deployable mechanisms for motion sensing. In order to investigate the effect of temperature and bending on the actuators' electrical resistance, an experiment was performed in four stages: 1) heating by using the environmental chamber, 2) bending, 3) cooling, and 4) recovery by resistive heating at ambient conditions. The experiment was performed using the setup described at the beginning of Section 2.3. The resistance was calculated using Ohm's and Pouillet's laws, see Equation (5):

$$R = \frac{V}{I} = \frac{\rho L}{A} \tag{5}$$

where R (Ω) is the resistance, V (V) is the voltage, I (A) is the current, ρ (Ω·m) is the resistivity, L (m) is the length, and A (m^2) is the cross-section area.

Fig. 5 presents typical results out of three tests that were performed. In each of the three tests, a pristine $SMPA_U$ sample was used only once. Fig. 5a shows the electrical resistance as a function of temperature in the 1st stage. During this stage, the $SMPA_U$ was heated while in its permanent shape using the environmental chamber of the universal testing system. As the $SMPA_U$ was heated to a temperature of 130 °C, its resistance was increased by 77% (from 66 Ω to 117 Ω), revealing the presence of two phases. The first phase shows a relatively small increase in resistance, from 66 Ω to 72 Ω, as the $SMPA_U$ was heated from RT to 110 °C. Above 110 °C, an abrupt resistance increase was observed, reaching 117 Ω at a temperature of 128 °C. While the first phase depicts a resistance change due to the change in the CF metallic conductivity, the second phase reflects an abrupt increase in resistance due to mechanical changes in the epoxy resin itself. This phenomenon has been previously observed for epoxy resins filled with CFs at various aspect ratios [46,47]. The actuator's semicrystalline CFs segments contain unordered plains of hexagonally arrayed sp^2 carbon atom sheets. Electrical current passes through the CF by π electrons, below and above these sheets (parallel to the basal *xy* plane). The mobility of the π electrons is similar to the behavior of electron gas in metals. During the first phase, while heating the SMPA in the environmental chamber, electron mobility decreased due to increased thermal vibrations of the atoms, i.e., collisions between the electrons and the phonons, and lattice irregularities, e.g., vacancies, resulting in smaller electron mean free path (MFP) [48]. The reason for the positive temperature coefficient (PTC) effect during the second phase is the breaking-off of inter-fiber contacts. The CFs embedded in the epoxy are composed of micron-sized filaments, with a minimal distance between them. When the polymer matrix shrinks during the curing and final cooling processes, a residual compressive strain is stored in the polymer gap between the fibers, as the CFs were pushed together. During heating, as the material becomes rubbery, the thermal expansion of the epoxy will compensate for the residual strain, and at a critical temperature it will lead to the separation of the fibers, thus lowering the number of inter-fiber contacts. Consequently, the temperature at which the PTC effect occurs is strongly dependent on the curing process. In this case, the epoxy was cured at 100 °C, followed by post-curing at 130 °C. The PTC effect started at an

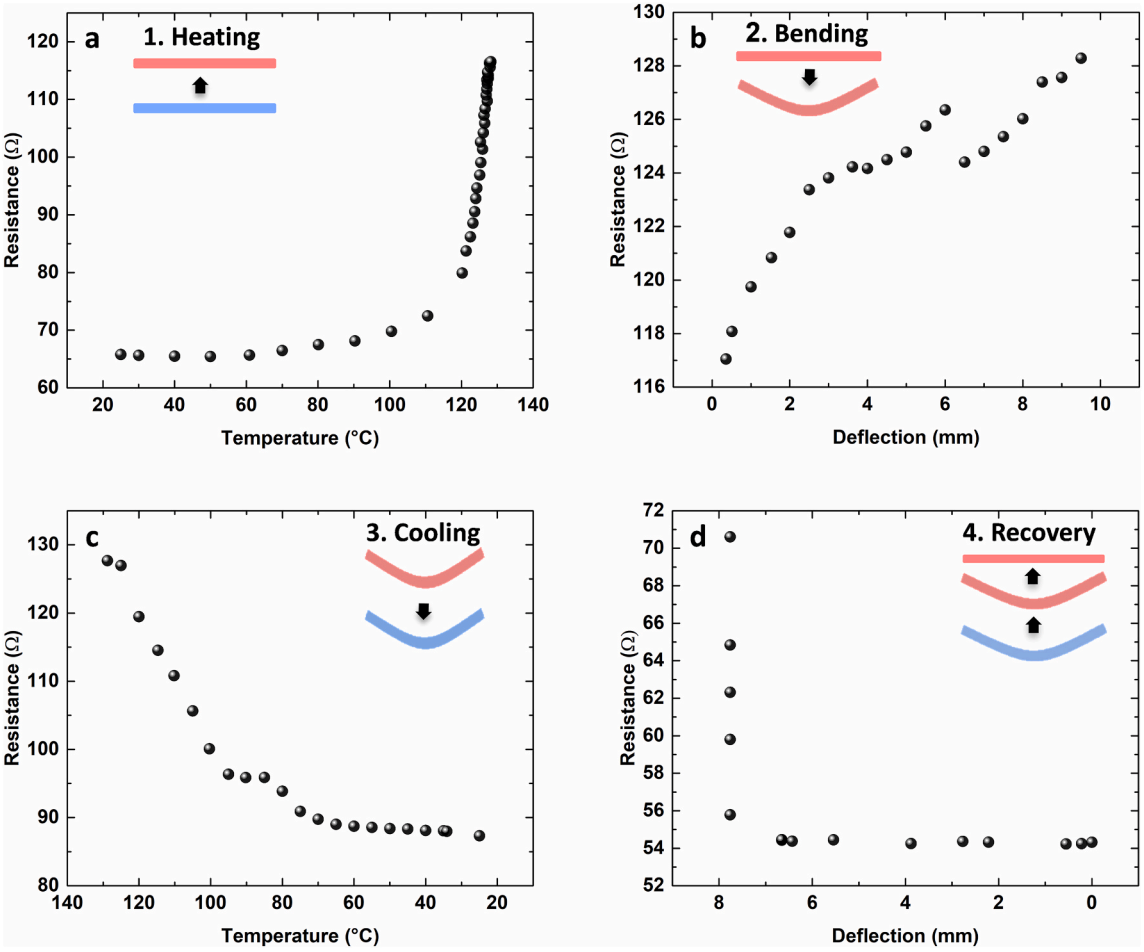

Fig. 5. (a) 1st-stage results. Resistance versus temperature during environmental chamber heating of the $SMPA_U$. (b) 2nd-stage results. Resistance versus deflection during bending of the preheated $SMPA_U$ at 130 °C. (c) 3rd-stage results. Resistance versus temperature during cooling of the $SMPA_U$. (d) 4th-stage results. Resistance versus deflection during recovery of the $SMPA_U$ by resistive heating.

intermediate temperature and was observed above 110 °C. Thus, during the 1st stage, the dominant mechanism that affected the $SMPA_U$ resistivity was electron scattering and reduction of inter-fiber contacts, which increased the resistivity during heating [49].

According to Equation (5), the resistance may also be affected by dimensional changes in the CF's length and cross-section area. In order to evaluate the influence of temperature on these parameters, the thermal expansion was calculated according to Equation (6):

$$\Delta L = L_0 \alpha \Delta T \tag{6}$$

where ΔL is the dimensional change, L_0 is the initial dimension, α is the coefficient of thermal expansion (CTE), and ΔT is the temperature change.

The CTE of the CF in the z-direction is extremely low and negative, $-4.1 \times 10^{-7}\ °C^{-1}$ [50]; it is about $2 \times 10^{-5}\ °C^{-1}$ in its x or y directions [48]. The length of the CF yarn is 260 mm per $SMPA_U$, whereas the typical cross-section area of a single fiber filament is 38.5 μm^2 [50]. Therefore, the fiber's longitudinal thermal dimensional change is 13.7 μm, merely 5×10^{-3}% change. The thermal expansion of the fiber's cross-section area was also minimal, only 0.2%. On the other hand, the CTE of a cured epoxy is $5–8 \times 10^{-5}\ °C^{-1}$, 2.5–4 times larger than that of CF, supporting the PTC phenomenon [51,52]. Thus, through the four stages of the SMPA recovery experiment, L was set constant, and in the 1st stage the cross-section area was considered constant too. Fig. 5b shows the results of the 2nd stage of resistance versus deflection measurements during bending of the $SMPA_U$ to its temporary u-like shape.

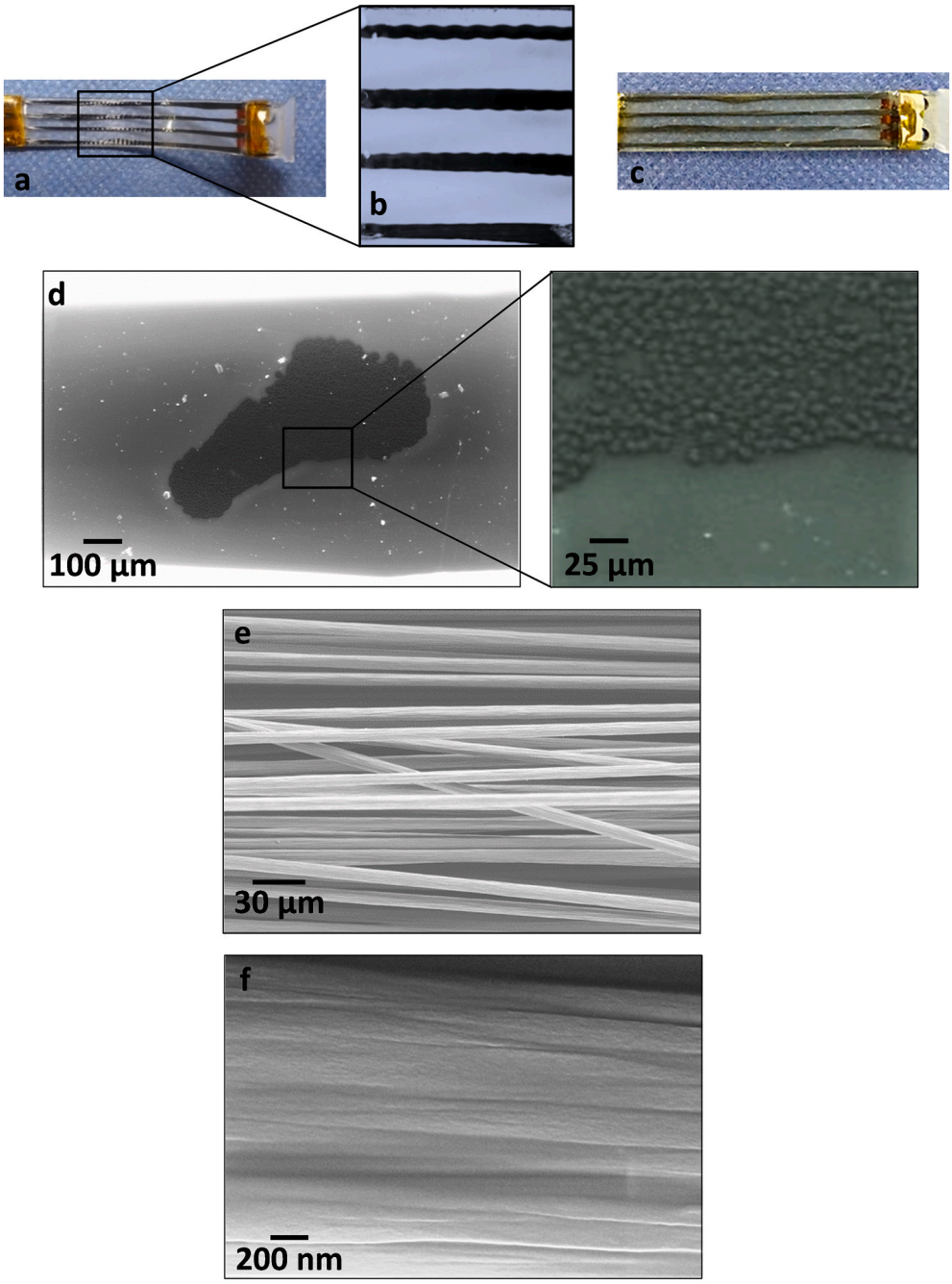

Fig. 6. (a) Concave side of $SMPA_U$ after bending to its temporary shape and cooling. (b) Buckling of the carbon fibers due to compression stress. (c) The $SMPA_U$ after recovery to its permanent planar shape. (d) Cross-section of an $SMPA_U$ – the carbon fiber yarn is embedded in the epoxy matrix. (e) Micro- and (f) nano-meter scale high-resolution scanning electron microscope images of carbon fibers.

An increase in the resistance by 9.1% (from 117 Ω to 128 Ω) was measured. This increase may be due to two possible reasons. First, either a sufficient number of fractured carbon monofilaments or disconnection of nearby filaments at specific points, due to bending, may lead to a lower cross-section area for electron current, if these filaments became electrically disconnected [53]. A second possible origin could be CF buckling deformation during the bending test [54–56], as shown in Fig. 6a and b. Buckling of the CF can occur if the fibers experience compression stresses [54]. Fig. 6d shows the cross-section of an $SMPA_U$. As shown, the CF yarn was embedded in the epoxy matrix in a manner that about half of the fibers were positioned above and the other half below the 1 mm thick sample centerline. Therefore, about half of the fibers in the yarn experienced compression stresses during bending of the $SMPA_U$. Buckling strains are proportional to the square root of the matrix-to-fiber modulus ratio. A typical ratio in which buckling occurs in comparable material systems is in the range of 0.01–0.05 [57]. The flexure modulus of the CF used in this work was 223 GPa [58]. The flexure modulus of the matrix was 2.3 GPa. Thus, the matrix-to-fiber modulus ratio of the matrix and fibers used in this work was 0.01. Therefore, the observation of buckling in this work fits nicely with the conditions for the formation of buckling of CF in composite materials and with the theory of buckling in general. In the *z*-direction (normal to the graphitic basal planes), the spacing between the graphite sheets presumably became larger due to the buckling. Hence, the electron tunneling transmission coefficient decreased, and higher resistance was measured as the electrons were forced to tunnel through a wider barrier to move from one graphite sheet to the other. Fig. 6e presents HRSEM images of the CFs, demonstrating the inter-fiber contact points between nearby filaments. Fig. 6f presents the HRSEM image of a single filament composed of interconnected fibrils having diameters of 100–200 nm. Fig. 5b also shows an abrupt resistance drop observed at a deflection value of 6 mm. This drop may be associated with a sudden increase in the friction between the $SMPA_U$ and the three-point bending supports during the bending. This could lead to a temporary local increase of the load, normal to the sample plane, that may result in a local temporary increase of nearby CF connecting points and to a local temporary decrease of the resistance.

Fig. 5c depicts the electrical resistance as a function of temperature in the 3rd stage during cooling of the $SMPA_U$ to RT in its temporary shape. During cooling, the resistance of the bent $SMPA_U$ was decreased by 32% (from 128 Ω to 87 Ω). During this cooling stage, residual stresses could lead to an opposite effect that could increase the actuator resistivity and, hence, its resistance. Upon cooling of the $SMPA_U$, residual stresses could form between the matrix and the fibers, and increase due to the shrinkage of the thermoset matrix around the fibers [59], thus increasing the buckling effect. However, the actual decrease in the resistance during cooling indicates that another, more dominant, process prevailed. This process concerns the reduction in electron-scattering events. At lower temperatures, fewer electron-scattering events occur and, hence, the resistivity and resistance decrease [48,49,60].

Fig. 5d depicts the 4th-stage results of resistance versus deflection measurements during recovery of the $AMPA_U$ to its permanent shape by gradual resistive heating. The resistive heating itself is a result of retarding forces and collisions involving charge carriers, usually electrons [60]. A drastic decrease in the resistance by 23% (from 70 Ω to 54 Ω) after deployment of less than 1 mm was observed. This drastic decrease may be attributed to two factors. First, when the $SMPA_U$ reached the T_g, the residual stresses and the buckling deformation were immediately released as SME started, leading to closer graphite aligned sheets, lowering the electron tunneling barrier width and, thus, lower resistivity was measured. Second, instant alternative connecting points were formed between the CFs during the deployment of the $SMPA_U$ in the initial deployment stage, which led to a higher cross-sectional area for electron current, hence, resulting in the decrease of the electrical resistivity and resistance. Fig. 6c demonstrates the disappearance of the CFs' buckling at the end of the SME. The phenomenon of an instant decrease in electrical resistance during the $SMPA_U$'s deployment may be used for motion sensing during the initial stage of the actuator deployment process while in space.

Fig. 7 presents a phenomenological model, which highlights the main parameters that influence the SMPA's resistance during bending, on the macro-, micro-, and nano-structure scales. This model demonstrates the structure-property dependency, which leads to the resistance decrease during deployment, by using three hierarchies: actuator level, CF macrostructure level, and graphite sheets molecular level. The actuator level depicts the permanent and the temporary shapes of the actuator, and the associated buckling effect. The CF macrostructure level shows the fibers in the aligned and buckled position. The circles around the monofilaments illustrate the monofilament-to-monofilament electrical contact points, and the rectangles show fractured monofilaments due to bending. In the permanent shape, a larger number of contact points exists between the monofilaments. During bending, the monofilaments are far apart, and some of them are fractured. The molecular level depicts the planes of graphite sheets in the carbon monofilament and the π electrons below and above these sheets. The distance between the sheets becomes larger ($L_{temporary} > L_{permanent}$) during bending, hence the electron tunneling barrier between the sheets increases.

Although heating *per se* increases the CFs' resistivity during recovery by resistive heating, the overall resistivity decreases sharply. The dominant parameters during recovery, which lead to this decrease in the resistance, are the increase in the number of the inter-fiber contacts and the reduction in the width of the tunneling barrier for electrons between the sheets.

3.3. The deployment kinetics of SMPAs under ambient and vacuum conditions

The dominant heat transfer mechanisms are different under ambient and vacuum conditions. At ambient pressure, the dominant mechanisms of heat transfer to the surrounding atmosphere are convection and conduction, while in vacuum the primary mechanism is radiation. The influence of the vacuum on the SMPAs' deployment kinetics was tested in order to simulate the UHV conditions in space. Furthermore, in order to improve the energetic efficiency of the SMPAs' deployment, a novel approach was developed, which is based on an internal reflectance heating mechanism. Implementation of this mechanism was done by coating the SMPAs with an aluminum coating. Aluminum offers high reflectivity in the near-IR spectrum and, hence, can be used as a solar reflector of the IR photons that are emitted during the resistive heating process.

$SMPA_U$ samples were deployed under both ambient and vacuum conditions, while $SMPA_{Al}$ samples were deployed only under vacuum conditions. Fig. 8 presents the recovery kinetic parameters of the various SMPAs under both ambient and vacuum conditions. Each curve is the average of three experiments. Fig. 8a depicts the SMPAs' deployment kinetics in terms of recovery angle change ($\Delta\theta$) versus time. The maximum bending angle was defined as $\Delta\theta = 0^\circ$. Fig. 8b shows the SMPAs' deployment kinetics in terms of $\Delta\theta$ versus the actuator's power consumption. Fig. 8c presents the angular velocity ($d\theta/dt$) versus deployment time, while Fig. 8d presents the SMPAs' electrical resistance versus $\Delta\theta$. Fig. 8a–c presents a general trend of almost immediate deployment that occurred after a certain dwell time in all three cases. The highest values of 310 s dwell time, 97 s recovery duration, and 2.46 W recovery power were observed at ambient pressure for the $SMPA_U$ samples. Performing the $SMPA_U$ deployment experiment under vacuum conditions resulted in moderate values of 224 s dwell time, 72 s recovery duration, and 1.53 W recovery power. The lowest values of 171 s dwell time, 71 s recovery duration, and 1.17 W recovery power were observed under vacuum conditions for the $SMPA_{Al}$ samples. These results prove the benefit of coating the SMPAs with aluminum, as deployment power consumption under vacuum conditions dropped by 24% thanks to this

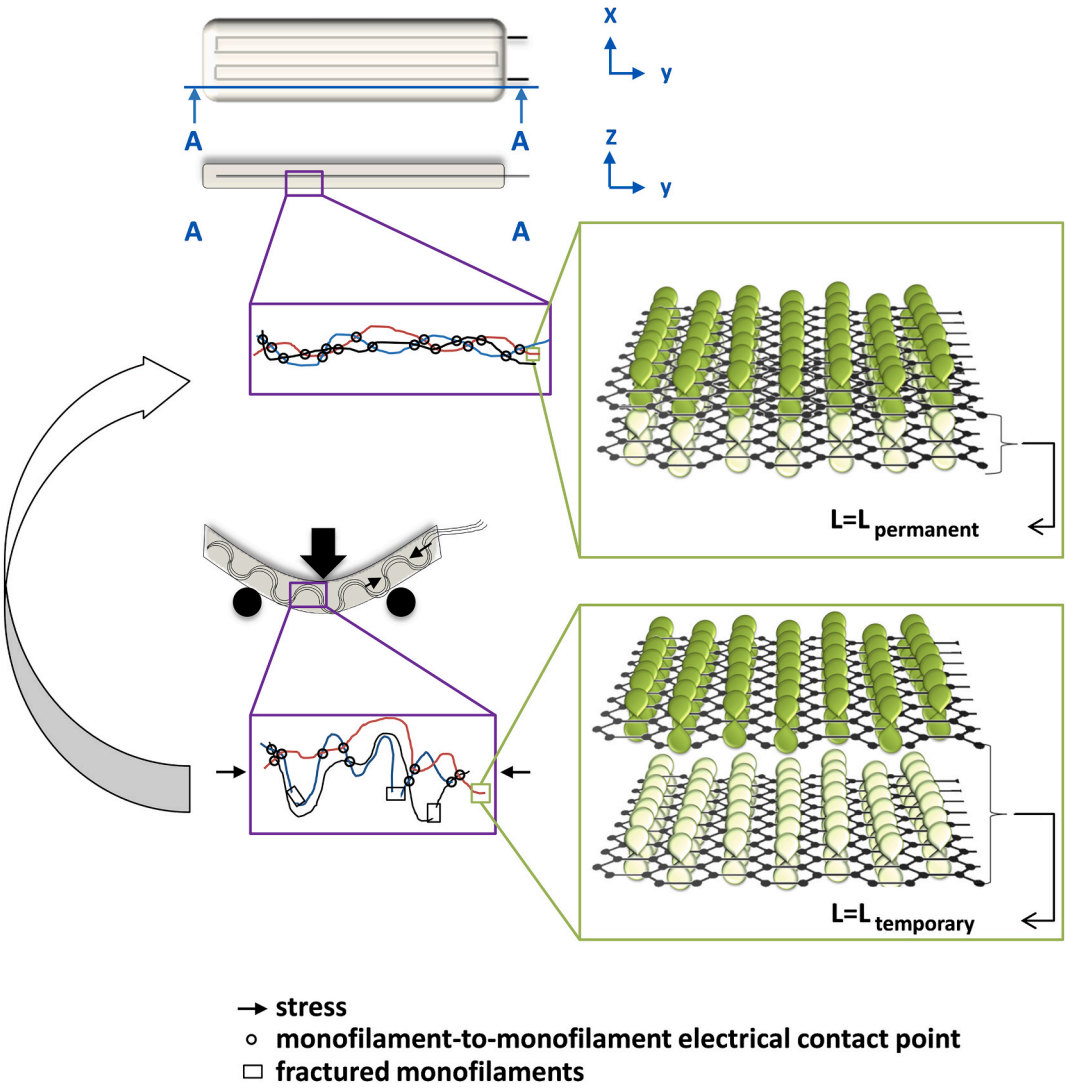

Fig. 7. A phenomenological model demonstrating the main parameters that influence the shape memory polymer actuator's electrical resistance during bending, on the macro-, micro-, and nano-structure scales.

process.

During the deployment stage, electrical current passes through the CFs and produces resistive heating. The current was set to produce a temperature of around 130 °C. According to Wein's law, at this temperature the emitted heat from the actuator has a typical wavelength of 7.2 μm. Under vacuum conditions, the $SMPA_{Al}$ preserved its temperature by internal radiative heating since the aluminum reflectivity at a wavelength of 7.2 μm is 98% [61]. In this process, the emitted photons were reflected into the bulk polymer by the solar reflective aluminum coating. Therefore, the aluminum coating preserved the temperature as a solar-reflective element and reduced the electric power consumption, as shown in Fig. 8b.

The final $\Delta\theta$ value of the $SMPA_U$ deployed in ambient conditions was 7° lower compared to the final $\Delta\theta$ value of the $SMPA_U$ and $SMPA_{Al}$ deployed in a vacuum environment, see Fig. 8a and b. In all these tests, the actuators returned to the 180° straight position. The difference in the final $\Delta\theta$ value is rather technical; the $SMPA_U$ samples deployed under ambient conditions were bent to a lower initial angle, to begin with, which exemplify the longer time it took these actuators to return to their permanent state.

The results presented in Fig. 8c show that at ambient pressure, the $SMPA_U$ had the longest dwell time, lowest angular velocity, and widest velocity distribution. In the vacuum environment, the maximum velocity was higher, and the distribution of the angular velocity was symmetric and narrow. These results indicate that the deployment in vacuum occurred at a short and specific timescale when reaching T_g. The deployment was even shorter for the $SMPA_{Al}$. The values of the angular velocity were 2.75°/s for the $SMPA_U$ deployed at ambient pressure and 3.5°/s and 6°/s for the $SMPA_U$ and $SMPA_{Al}$, respectively, deployed under vacuum environment.

Fig. 8d shows the electrical resistance versus recovery angle change of the $SMPA_U$ and $SMPA_{Al}$ samples under ambient and vacuum conditions. A sharp decrease in the resistance at the beginning of the deployment and a moderate decrease during the rest of the deployment are evident. Furthermore, the highest resistance was obtained under vacuum conditions for the $SMPA_{Al}$. The lowest resistance was measured under ambient conditions for the $SMPA_U$. The decrease in the actuator's resistance was due to the release of the buckling deformation and the residual stresses, as analyzed previously in Section 3.2. The higher the temperature of the SMPA, the higher its resistance, as shown in Fig. 5a. The $SMPA_{Al}$ operated under vacuum conditions reached the highest temperature due to internal IR reflections, and therefore showed the highest measured resistance. The $SMPA_U$, operated under ambient conditions, reached the lowest temperature due to heat losses by convection and conduction to the surrounding atmosphere, and therefore showed the lowest measured resistance.

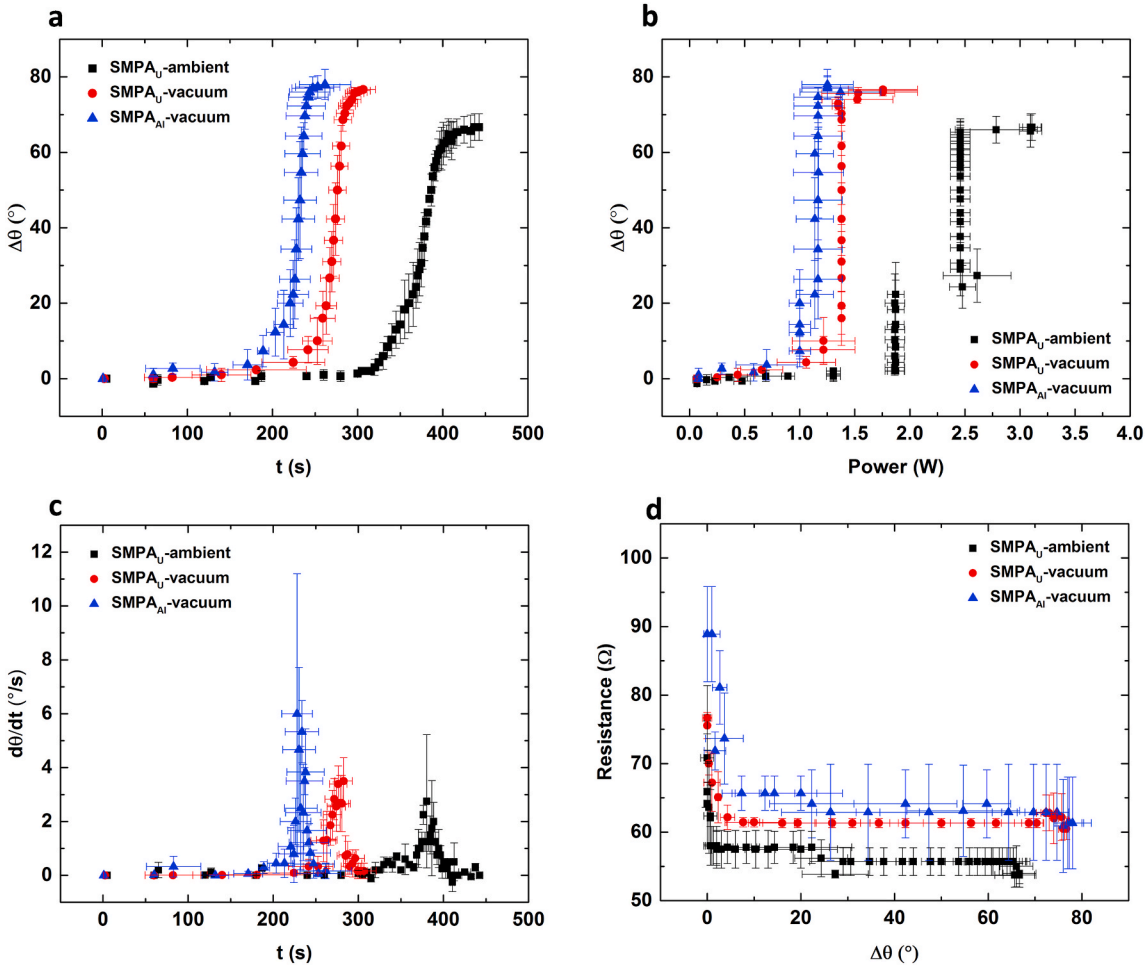

Fig. 8. Recovery of $SMPA_U$ and $SMPA_{Al}$ samples under ambient and vacuum conditions. (a) Recovery angle change ($\Delta\theta$) versus deployment time. (b) $\Delta\theta$ versus deployment power. (c) Angular velocity versus deployment time. (d) Resistance versus $\Delta\theta$.

3.4. Durability and prospect for using SMPA in space

In order to use the SMPA in space it should be able to operate under the harsh conditions of space. One of the greatest concerns regarding operation of SMP-based actuators in space is overheating, which can cause inadvertent spontaneous deployment before schedule. In order to use the SMPA in space, it needs to be painted with a commercial space-qualified white paint, a common method to control and lower its temperature and to protect it from the space environment [62,63]. The steady-state temperature of the SMPA can be expressed by the following energy balance equation [62,64]:

$$T = \left(\frac{SA_s\alpha_s}{\varepsilon A\sigma}\right)^{\frac{1}{4}} \tag{7}$$

where T is the absolute temperature, S is the solar constant, σ is the Stefan–Boltzmann constant, A_s is the projected surface area perpendicular to solar rays, A is the total surface area, α is the solar absorptance, and ε is the thermal emittance of the exposed surface.

According to Equation (7) and the thermo-optical properties of typical space-qualified white paints, the expected temperature of a painted SMPA will reach a maximum of ~10 °C [62]. As shown in Fig. 4a, the epoxy used in this work maintains its original mechanical properties up to 80 °C, and its T_g is 102 °C. Therefore, in terms of thermal balance in orbit, since the difference between the maximum temperature and the triggering temperature of the SMPA is ~70 °C, controlling the SMPA surface temperature with white paint resolves issues such as spontaneous and unintentional deployment, and would maintain the SMPA's fixity and recovery. In LEO, the SMPA may be exposed to AO [65]. The erosion yield of an unprotected organic material, Kapton H for example, is 3.0×10^{-24} cm^3/O-atom [66]. However, the erosion yield of silicone-based white paint exposed to both AO and vacuum UV is merely 9.1×10^{-26} cm^3/O-atom [67]. Therefore, applying a white paint on the SMPA's surface not only lowers its temperature, but also provides protection from AO and UV. As AO and UV cause only surface effects, their impact on the mechanical and shape memory properties of the SMPA should be negligible [68]. For a typical space mission of seven years, a spacecraft orbiting at 2000 km with 60° inclination will be exposed to a total dose of 100–230 krad [69]. However, the mechanical properties of epoxies exposed to an ionizing radiation dose as high as 3.2 Mrad were not affected by the radiation [70]. Therefore, the exposure of the SMPA to ionizing radiation in space will not affect its mechanical or shape memory properties, as the damage threshold of epoxy is higher than the expected dose in a typical mission in space. Unprotected SMPA may suffer overheating and erosion by the space environment. However, by choosing available commercial protective coatings, our SMPA can be well-suited for future space applications.

4. Summary and conclusions

Unique SMPs and SMPAs, based on CFs and epoxy matrix, were designed as building blocks for future space applications and lightweight deploying mechanisms. Their mechanical and electrical

properties, as well as their SME parameters in vacuum environment, were evaluated.

The deployment process in space requires motion sensing. During resistive heating and deployment, a rapid decrease in the $SMPA_U$ electrical resistance was noticed. This phenomenon was caused by the temperature effect and $SMPA_U$ deflection state. As the $SMPA_U$ deployed, the CFs abruptly unbuckled, compression stresses were released, and new electrical connecting points were formed between the fibers. Thus, CFs can serve not only as heating elements and for mechanical reinforcement, but also as motion sensing for the initial stage of deployment in space. A phenomenological model which links all of the above findings was suggested to explain this phenomenon.

Energy consumption is critical in space applications and needs to be brought to a minimum, as power budget in spacecraft is limited. The SME properties of $SMPA_U$ and $SMPA_{Al}$ were measured under ambient and vacuum conditions. When the $SMPA_{Al}$ was deployed in a vacuum environment, its reflective nanometric aluminum coating preserved the temperature more efficiently than $SMPA_U$. The reason for this is an internal radiative heating process, as photons were reflected into the bulk polymer. In this manner, a reduction of 24% in the electrical power consumption during the deployment process was observed, compared to that of the $SMPA_U$. The deposition of the aluminum thermal coating also caused the $SMPA_{Al}$ to deploy faster and in a uniform manner, compared to the $SMPA_U$. The durability of the SMPAs in the space environment was discussed, and means to improve it were given, adapting existing commercial solutions.

This work demonstrates the great potential of SMPAs based on epoxy with embedded CFs for use in future space applications.

Declaration of competing interest

The authors declare that they have no known competing financial interests or personal relationships that could have appeared to influence the work reported in this paper.

Acknowledgments

The authors would like to thank Dr. N. Atar, M. Ozeri, E.R. Wallach, G. Strum, N. Refaeli, and R. Naim from Soreq NRC for their technical support and advice. We also thank the Israel Department of Defense for funding this project (grant #4440826405).

References

[1] I. Gouzman, E. Grossman, R. Verker, N. Atar, A. Bolker, N. Eliaz, Advances in polyimide-based materials for space applications, Adv. Mater. 31 (2019) 1807738.
[2] R. Verker, N. Eliaz, I. Gouzman, S. Eliezer, M. Fraenkel, S. Maman, F. Beckmann, K. Pranzas, E. Grossman, The effect of simulated hypervelocity space debris on polymers, Acta Mater. 52 (2004) 5539–5549.
[3] R. Verker, E. Grossman, I. Gouzman, N. Eliaz, Residual stress effect on degradation of polyimide under simulated hypervelocity space debris and atomic oxygen, Polymer 48 (2007) 19–24.
[4] R. Verker, E. Grossman, I. Gouzman, N. Eliaz, POSS-polyimide nanocomposite films: simulated hypervelocity space debris and atomic oxygen effects, High Perform. Polym. 20 (2008) 475–491.
[5] R. Verker, E. Grossman, N. Eliaz, Erosion of POSS-polyimide films under hypervelocity impact and atomic oxygen: the role of mechanical properties at elevated temperatures, Acta Mater. 57 (2009) 1112–1119.
[6] R. Verker, E. Grossman, I. Gouzman, N. Eliaz, TriSilanolPhenyl POSS-polyimide nanocomposites: structure-properties relationship, Compos. Sci. Technol. 69 (2009) 2178–2184.
[7] R. Verker, E. Grossman, N. Eliaz, Effect of the POSS-Polyimide nanostructure on its mechanical and electrical properties, Compos. Sci. Technol. 72 (2012) 1408–1415.
[8] J. Anderson, R.E. Smith, Natural orbital environment guidelines for use in aerospace vehicle development, NASA Tech. Memo. 4527 (1994).
[9] J.P. Raymond, E.G. Stassinopoulos, Space radiation environment for electronics, Proc. IEEE 76 (1988) 1423–1442.
[10] E. Grossman, I. Gouzman, Space environment effects on polymers in low earth orbit, Nucl. Instrum. Methods Phys. Res. Sect. B Beam Interact. Mater. Atoms 208 (2003) 48–57.
[11] R. Verker, A. Bolker, Y. Carmiel, I. Gouzman, E. Grossman, T.K. Minton, S. Remaury, Ground testing of an on-orbit atomic oxygen flux and ionizing radiation dose sensor based on material degradation by the space environment, Acta Astronaut. 173 (2020 August) 333–343.
[12] R.H. Pater, P.A. Curto, Advanced materials for space applications, Acta Astronaut. 61 (2007) 1121–1129.
[13] F. Li, Y. Liu, J. Leng, Progress of shape memory polymers and their composites in aerospace applications, Smart Mater. Struct. 28 (2019) 103003.
[14] M.J. Jo, H. Choi, H. Jang, W.-R. Yu, M. Park, Y. Kim, J.K. Park, J.H. Youk, Preparation of epoxy-based shape memory polymers for deployable space structures using diglycidyl ether of ethoxylated bisphenol-A, J. Polym. Res. 26 (2019) 129.
[15] J. Fan, G. Li, High enthalpy storage thermoset network with giant stress and energy output in rubbery state, Nat. Commun. 9 (2018) 642.
[16] C. Liu, H. Qin, P.T. Mather, Review of progress in shape-memory polymers, J. Mater. Chem. 17 (2007) 1543.
[17] H. Tobushi, S. Hayashi, Y. Sugimoto, K. Date, Two-way bending properties of shape memory composite with SMA and SMP, Materials 2 (2009) 1180–1192.
[18] X. Zheng, S. Zhou, X. Li, J. Weng, Shape memory properties of poly(d,l-lactide)/hydroxyapatite composites, Biomaterials 27 (2006) 4288–4295.
[19] J. Leng, X. Lan, Y. Liu, S. Du, Shape-memory polymers and their composites: stimulus methods and applications, Prog. Mater. Sci. 56 (2011) 1077–1135.
[20] M. Behl, A. Lendlein, Shape-memory polymers, Mater. Today 10 (2007) 20–28.
[21] Y. Liu, H. Du, L. Liu, J. Leng, Shape memory polymers and their composites in aerospace applications: a review, Smart Mater. Struct. 23 (2014) 23001.
[22] Y. Wu, J. Hu, C. Zhang, J. Han, Y. Wang, B. Kumar, A facile approach to fabricate a UV/heat dual-responsive triple shape memory polymer, J. Mater. Chem. A. 3 (2015) 97–100.
[23] H. Koerner, R.J. Strong, M.L. Smith, D.H. Wang, L.-S. Tan, K.M. Lee, T.J. White, R. A. Vaia, Polymer design for high temperature shape memory: low crosslink density polyimides, Polymer 54 (2013) 391–402.
[24] M. Loeblein, A. Bolker, Z.L. Ngoh, L. Li, E. Wallach, S.H. Tsang, M. Pawlik, R. Verker, N. Atar, I. Gouzman, E.H.T. Teo, Novel timed and self-resistive heating shape memory polymer hybrid for large area and energy efficient application, Carbon 139 (2018) 626–634.
[25] A.J.W. McClung, G.P. Tandon, K.E. Goecke, J.W. Baur, Non-contact technique for characterizing full-field surface deformation of shape memory polymers at elevated and room temperatures, Polym. Test. 30 (2011) 140–149.
[26] E.R. Abrahamson, M.S. Lake, N.A. Munshi, K. Gall, Shape memory mechanics of an elastic memory composite resin, J. Intell. Mater. Syst. Struct. 14 (2003) 623–632.
[27] E.J. Friebele, C.G. Askins, A.B. Bosse, A.D. Kersey, H.J. Patrick, W.R. Pogue, M. A. Putnam, W.R. Simon, F.A. Tasker, W.S. Vincent, S.T. Vohra, Optical fiber sensors for spacecraft applications, Smart Mater. Struct. 8 (1999) 813–838.
[28] G. Sala, L. Di Landro, A. Airoldi, P. Bettini, Fibre optics health monitoring for aeronautical applications, Meccanica 50 (2015) 2547–2567.
[29] S. Bandyopadhyay, R. Foust, G.P. Subramanian, S.-J. Chung, F.Y. Hadaegh, Review of formation flying and constellation missions using nanosatellites, J. Spacecraft Rockets 53 (2016) 567–578.
[30] E. Shakhmatov, I. Belokonov, I. Timbai, E. Ustiugov, A. Nikitin, S. Shafran, SSAU project of the nanosatellite SamSat-QB50 for monitoring the Earth's thermosphere parameters, Procedia Eng 104 (2015) 139–146.
[31] C.K. Pang, A. Kumar, C.H. Goh, C.V. Le, Nano-satellite swarm for SAR applications: design and robust scheduling, IEEE Trans. Aero. Electron. Syst. 51 (2015) 853–865.
[32] E. Clements, R. Aniceto, D. Barnes, D. Caplan, J. Clark, I. Del Portillo, C. Haughwout, M. Khatsenko, R. Kingsbury, M. Lee, R. Morgan, J. Twichell, K. Riesing, H. Yoon, C. Ziegler, K. Cahoy, Nanosatellite optical downlink experiment: design, simulation, and prototyping, Opt. Eng. 55 (2016).
[33] B. Perret, B. Schartel, K. Stöß, M. Ciesielski, J. Diederichs, M. Döring, J. Krämer, V. Altstädt, A new halogen-free flame retardant based on 9,10-dihydro-9-oxa-10-phosphaphenanthrene-10-oxide for epoxy resins and their carbon fiber composites for the automotive and aviation industries, Macromol. Mater. Eng. 296 (2011) 14–30.
[34] S.Y. Park, H.S. Choi, W.J. Choi, H. Kwon, Effect of vacuum thermal cyclic exposures on unidirectional carbon fiber/epoxy composites for low Earth orbit space applications, Compos. B Eng. 43 (2012) 726–738.
[35] J.D.H. Hughes, The carbon fibre/epoxy interface—a review, Compos. Sci. Technol. 41 (1991) 13–45.
[36] R. Bacon, Growth, structure, and properties of graphite whiskers, J. Appl. Phys. 31 (1960) 283–290.
[37] M. Kim, D.H. Sung, K. Kong, N. Kim, B.-J. Kim, H.W. Park, Y.-B. Park, M. Jung, S. H. Lee, S.G. Kim, Characterization of resistive heating and thermoelectric behavior of discontinuous carbon fiber-epoxy composites, Compos. B Eng. 90 (2016) 37–44.
[38] C. Joseph, C. Viney, Electrical resistance curing of carbon-fibre/epoxy composites, Compos. Sci. Technol. 60 (2000) 315–319.
[39] I.S. Gunes, G.A. Jimenez, S.C. Jana, Carbonaceous fillers for fhape memory actuation of polyurethane composites by resistive heating, Carbon N. Y. 47 (2009) 981–997.
[40] S.C. Bennett, D.J. Johnson, Strength structure relationships in PAN-based carbon fibres, in: 5th London Int. Carbon Graph. Conf., Society of Chemical Industry, London, 1978, p. 377.
[41] T. Xie, I.A. Rousseau, Facile tailoring of thermal transition temperatures of epoxy shape memory polymers, Polymer 50 (2009) 1852–1856.
[42] ASTM D790-00, Standard Test Methods for Flexural Properties of Unreinforced and Reinforced Plastics and Electrical Insulating Materials, ASTM International, West Conshohocken, PA, 2002.
[43] D. Ratna, J. Karger-Kocsis, Recent advances in shape memory polymers and composites: a review, J. Mater. Sci. 43 (2008) 254–269.

[44] K. Kratz, R. Habermann, T. Becker, K. Richau, A. Lendlein, Shape-memory properties and degradation behavior of multifunctional electro-spun scaffolds, Int. J. Artif. Organs 34 (2011) 225–230.
[45] A.B. Leonardi, L.A. Fasce, I.A. Zucchi, C.E. Hoppe, E.R. Soulé, C.J. Pérez, R.J. J. Williams, Shape memory epoxies based on networks with chemical and physical crosslinks, Eur. Polym. J. 47 (2011) 362–369.
[46] Y. Chekanov, R. Ohnogi, S. Asai, M. Sumita, Positive temperature coefficient effect of epoxy resin filled with short carbon fibers, Polym. J. 30 (1998) 381–387.
[47] W. Di, G. Zhang, Resistivity-temperature behavior of carbon fiber filled semicrystalline composites, J. Appl. Polym. Sci. 91 (2004) 1222–1228.
[48] H.O. Pierson, Handbook of Carbon, Graphite, Diamonds and Fullerenes: Processing, Properties and Applications, William Andrew, 2012.
[49] C.L. Kane, E.J. Mele, R.S. Lee, J.E. Fischer, P. Petit, H. Dai, A. Thess, R.E. Smalley, A.R.M. Verschueren, S.J. Tans, C. Dekker, Temperature-dependent resistivity of single-wall carbon nanotubes, Europhys. Lett. 41 (1998) 683–688.
[50] Torayca®, T300 Technical Data Sheet No. CFA-001, 2018. https://www.toraycma.com/page.php?id=661.
[51] M.J. Adamson, Thermal expansion and swelling of cured epoxy resin used in graphite/epoxy composite materials, J. Mater. Sci. 15 (1980) 1736–1745.
[52] J.R. Strife, K.M. Prewo, The thermal expansion behavior of unidirectional and bidirectional kevlar/epoxy composites, J. Compos. Mater. 13 (1979) 264–277.
[53] P.E. Irving, C. Thiagarajan, Fatigue damage characterization in carbon fibre composite materials using an electrical potential technique, Smart Mater. Struct. 7 (1998) 456–466.
[54] K. Gall, M. Mikulas, N.A. Munshi, F. Beavers, M. Tupper, Carbon fiber reinforced shape memory polymer composites, J. Intell. Mater. Syst. Struct. 11 (2000) 877–886.
[55] O. Lourie, D.M. Cox, H.D. Wagner, Buckling and collapse of embedded carbon nanotubes, Phys. Rev. Lett. 81 (1998) 1638–1641.
[56] X. Lan, L. Liu, Y. Liu, J. Leng, S. Du, Post microbuckling mechanics of fibre-reinforced shape-memory polymers undergoing flexure deformation, Mech. Mater. 72 (2014) 46–60.
[57] H.T. Hahn, M.M. Sohi, Buckling of a fiber bundle embedded in epoxy, Compos. Sci. Technol. 27 (1986) 25–41.
[58] K. Naito, Y. Tanaka, J.-M. Yang, Y. Kagawa, Flexural properties of PAN- and pitch-based carbon fibers, J. Am. Ceram. Soc. 92 (2009) 186–192.
[59] J.A. Nairn, C.-H. Liu, D.-A. Mendels, S. Zhandarov, Fracture mechanics analysis of the single-fiber pull-out test and the microbond test including the effects of friction and thermal stresses, in: Proceeding 16th Annu. Technol. Conf. Am. Soc. Compos., Citeseer, 2001.
[60] A. Von Meier, A Conceptual Introduction - Electric Power Systems, in: Wiley Online Library, 2006.
[61] H. Tups, K. Syassen, Effect of pressure on the optical absorption in aluminium, J. Phys. F Met. Phys. 14 (1984) 2753–2767.
[62] A.K. Sharma, N. Sridhara, Degradation of thermal control materials under a simulated radiative space environment, Adv. Space Res. 50 (2012) 1411–1424.
[63] S. Remaury, P. Nabarra, E. Bellouard, S. D'Escrivan, In-flight aging of thermal coatings: THERME experiment, J. Spacecraft Rockets 48 (2011) 27–33.
[64] A.C. Tribble, The Space Environment: Implications for Spacecraft Design-Revised, and Expanded Edition, Princeton University Press, 2003.
[65] J.I. Kleiman, Z.A. Iskanderova, Y.I. Gudimenko, W.D. Morison, R.C. Tennyson, Polymers and composites in the low earth orbit space environment: interaction and protection, Can. Aeronaut. Space J. 45 (1999) 148–160.
[66] B.A. Banks, J.A. Backus, M. V Manno, D.L. Waters, K.C. Cameron, K.K. de Groh, Atomic Oxygen Erosion Yield Prediction for Spacecraft Polymers in Low Earth Orbit, 2009. NASA/TM-2009-215812; E-17074.
[67] I. Gouzman, E. Grossman, G. Lempert, Y. Noter, Y. Lifshitz, V. Viel-Inguimbert, M. Dinguirard, Atomic oxygen durability of a silicone paint: a comparison between two simulation methods, J. Spacecraft Rockets 41 (2004) 350–355.
[68] Q. Tan, F. Li, L. Liu, H. Chu, Y. Liu, J. Leng, Effects of atomic oxygen on epoxy-based shape memory polymer in low earth orbit, J. Intell. Mater. Syst. Struct. 29 (2017) 1081–1087.
[69] J. Arnous, J. Edwards, Y. Kinashi, Natural space radiation effects on representative space-based systems, in: AIAA Sp. Programs Technol. Conf. Exhib. 1993, 1993. Huntsville, AL, United states.
[70] J. Zimmermann, M.Z. Sadeghi, K.U. Schroeder, Exposure of structural epoxy adhesive to combination of tensile stress and γ-radiation, Int. J. Adhesion Adhes. 97 (2020) 102496.